Nuclear mass table in deformed relativistic Hartree-Fock Bogoliubov model with localized exchange terms*

Y. N. Huang (黄亚男)[1,2] P. Li (李鹏)[1,2] Q. Zhao (赵强)[3,4†] Y. F. Niu (牛一斐)[5‡]

[1]School of Nuclear Science and Technology, Lanzhou University, Lanzhou 730000, China
[2]Frontier Science Center for Rare Isotopes, Lanzhou University, Lanzhou 730000, China
[3]China Institute of Atomic Energy, P.O. Box 275, Beijing 102413, China
[4]Center for Exotic Nuclear Studies, Institute for Basic Science, Daejeon 34126, South Korea
[5]School of Physics and Astronomy, Shanghai Key Laboratory for Particle Physics and Cosmology, and Key Laboratory for Particle Astrophysics and Cosmology (MoE), Shanghai Jiao Tong University, Shanghai 200240, China

Abstract: The nuclear landscape is investigated within the localized axially deformed relativistic Hartree-Fock-Bogoliubov (DRHFB) theory using the density-dependent point-coupling functional PCF-PK1, in which exchange terms are incorporated through the Fierz transformation. Ground-state properties, including deformations, binding energies, drip lines, charge radii, and α-decay energies, are analyzed and compared with experimental data and results from other functionals. In deformed calculations for nuclei with $8 \leq Z \leq 120$, 7550 nuclei are predicted to be bound, with an root-mean-square (rms) deviation of 2.882 MeV for binding energies. This deviation is reduced to 1.721 MeV when rotational corrections are included. The predicted drip-line positions agree better with experiment than those obtained in the spherical case, and the charge radii are reproduced with an rms deviation of 0.0298 fm for 1010 experimental data points. Including deformation reduces the rms deviation of Q_α from 1.6263 MeV to 0.7215 MeV, and it becomes 0.7511 MeV when rotational corrections are further included. The removal of the spurious shell closures at $Z = 58$ and 92 is examined using shell gaps. In the superheavy region, the neutron magic numbers $N = 162$, 184, and 308 are predicted, whereas no pronounced proton magic number is found. To further improve the mass accuracy, a neural-network approach based on a gated recurrent unit is adopted to correct the mass residuals along isotopic and isotonic chains, reducing the rms deviation of the binding energies to 0.089 MeV.

Keywords: Nuclear mass, Relativistic Hartree-Fock Bogoliubov theory, Fierz transformation, Axial deformation, Neural network

DOI: 10.1088/1674-1137/aebba0 **CSTR:**

CPC Accepted

I. INTRODUCTION

Nuclear mass, as the most fundamental property of atomic nuclei, is crucial for understanding the nucleon-nucleon interaction [1, 2], nuclear structure phenomena such as magic numbers [3], nuclear halos [4], and exotic shapes [5], the origin of heavy elements [6], among others. It has been suggested that about half of the heavy elements beyond iron are synthesized by the rapid-neutron capture process (r-process) [7]. However, simulations of r-process nucleosynthesis require the nuclear masses of thousands of nuclei, most of which lie on the neutron-rich side [8]. Experimentally, masses have been measured for about 2800 nuclei [9, 10]. Therefore, theoretical studies are needed to provide nuclear masses beyond current experimental reach.

Considerable efforts have been devoted to describing nuclear masses using macroscopic-microscopic (mac-mic) and microscopic models. Among mac-mic models, the WS4 mass formula achieves an accuracy of 298 keV [11], and the finite-range droplet model (FRDM) provides an accuracy of 560 keV [12]; both are widely used in r-process simulations [13, 14]. However, the extrapolation capabilities of mac-mic models are limited for nuclei away from the β-stability line. In contrast, microscopic models are generally considered to have better ex-

Received 14 September 2026; Accepted 30 October 2026

* This work is supported by the National Key Research and Development (R&D) Program under Grant No. 2021YFA1601500, the National Natural Science Foundation of China under Grant No. 12075104, No. 12147101, and No. 12447106, the Fundamental Research Funds for the Central Universities lzujbky-2023-stlt01, the Institute for Basic Science funded by the Korean government (Grant No. IBS-R031-D1), the funding of the China Institute of Atomic Energy (Grants No. YC010270525794 and No. PA010271225779), the Lingchuang Research Project of China National Nuclear Corporation under Grant No. CNNC-LCKY-2024-082, and the Science and Technology Innovation Leading Talent Project of Gansu Province (Project No. 25RCKA025)

† E-mail: zhaoqiang@ciae.ac.cn
‡ E-mail: niuyf@sjtu.edu.cn

©2027 Chinese Physical Society and the Institute of High Energy Physics of the Chinese Academy of Sciences and the Institute of Modern Physics of the Chinese Academy of Sciences and IOP Publishing Ltd. All rights, including for text and data mining, AI training, and similar technologies, are reserved.

trapolation ability. Based on the Skyrme Hartree-Fock-Bogoliubov (SHFB) framework, the HFB-1 to HFB-32 mass models have achieved remarkable success, reaching an accuracy of about 500 keV [15, 16]. The uncertainties of the drip lines have also been studied within the SHFB framework [17], highlighting the need for a global description that extends beyond experimental reach. The Gogny HFB model also provides a mass formula with an accuracy of 798 keV [18].

Among microscopic models, covariant density functional theory (CDFT) has attracted wide attention because of its unique advantages [19]. It naturally introduces spin-orbit coupling [20−22], provides an essential explanation for pseudospin symmetry [23], and self-consistently includes time-odd fields [24], making it widely applied in nuclear mass-table studies. The binding energies of 7373 nuclei were calculated based on the spherical relativistic Hartree-Bogoliubov (RHB) theory using PC-L3R, yielding a root-mean-square (rms) deviation of 1.339 MeV with respect to experimental data for 91 spherical nuclei [25]. For weakly bound nuclei near the drip line, continuum effects become essential. Within the relativistic continuum Hartree-Bogoliubov (RCHB) theory, PC-PK1 was adopted under the spherical approximation to construct the first mass table that incorporates continuum effects [26], which reaches an accuracy of 8.143 MeV with respect to 2347 nuclei.

Most nuclei in the nuclear chart are deformed. Deformation plays a vital role in nuclear ground-state properties, such as binding energies and radii [27], as well as in nuclear fission, collective motion, and other phenomena [28]. Early deformed relativistic mean-field (RMF) calculations for even-even nuclei were performed using the TMA functional, and the rms deviation is 2.71 MeV [29]. However, pairing correlations were ignored, which led to unreasonable *r*-process abundance peaks [29]. Pairing effects are essential for nuclear masses, for example, to reproduce the odd-even mass difference [30]. Subsequently, a mass table for even-even nuclei was constructed based on the deformed RMF + Bardeen-Cooper-Schrieffer (BCS) theory using the NL3 functional, yielding an accuracy of 2.6 MeV [31]. The entire nuclear chart with $Z,N \geq 8$ and $Z \leq 100$ was later described based on the deformed RMF + BCS theory using TMA, giving an rms deviation of 2.118 MeV [32]. For nuclei far from the valley of stability, the BCS method may fail, and the Bogoliubov transformation provides a more reasonable description. The functionals DD-ME2, DD-PC1, DD-MEδ, and NL3* were applied to test theoretical predictions for even-even nuclei in the range $Z \leq 104$ [33, 34] and later in the superheavy region with $100 \leq Z \leq 130$ [35] using the axially deformed RHB (DRHB) theory. The predictions give an accuracy of about 2 MeV [33, 34]. To provide a more reasonable description near drip lines, the deformed relativistic Hartree-Bogoliubov in continuum (DRHBc) theory was developed [36, 37] in the nonlinear meson-exchange framework. The point-coupling DRHBc theory was further developed [38, 39] to construct a mass table that incorporates both deformation and continuum effects. It has already been applied to even-even [40] and even-*Z* nuclei [41] using PC-PK1, achieving accuracies of 1.518 MeV and 1.433 MeV, respectively. Apart from axial deformation, triaxial deformation has also been considered within RHB calculations using PC-PK1, in which even-even nuclei in the range $8 \leq Z \leq 104$ have been studied, and the accuracy is improved to 1.31 MeV [42]. Notably, no global fits to nuclear masses or phenomenological corrections are applied in the above studies, in contrast to the Skyrme or Gogny mass formulas.

The above applications of CDFT neglect the Fock terms. The inclusion of Fock terms is essential for incorporating the one-pion exchange process and tensor correlations [43], which substantially improves the description of shell-structure evolution [44] and restores pseudospin symmetry [45]. However, the high computational cost hinders its widespread application. To overcome this limitation, the Fock terms were expressed as direct terms via a Fierz transformation in the relativistic point-coupling model [46], an approach that has been implemented in the PCF-PK1 functional [47].

Apart from Fock terms, spurious shells at $Z = 58$ and 92 exist in general CDFT predictions, leading to the overestimation of binding energies near ^{140}Ce and ^{218}U [48]. This issue has been investigated within both the RHF and RMF frameworks, and the studies indicate that the density dependence of the σ and ω coupling constants plays a key role [45, 49]. For the PCF-PK1 functional, the constraint $f_S''(1) = f_V''(1)$ on the density-dependent functions of the scalar and vector channels was released during parameter optimization, which, in combination with the tensor coupling, leads to the removal of the spurious shells [47].

Therefore, the PCF-PK1 functional, which includes Fock terms and tensor coupling, offers an alternative approach to nuclear mass predictions. As a first step, PCF-PK1 was tested under the spherical approximation for predicting nuclear ground-state properties and describing shell structure [50]. One notable success is that PCF-PK1 removes the spurious shells at $Z = 58$ and 92 within the localized RHFB framework. The natural extension is therefore to lift the spherical approximation and examine how these shell-structure features of PCF-PK1 behave in deformed nuclei. To address this, we perform localized DRHFB calculations using PCF-PK1 for nuclei with $8 \leq Z \leq 120$ and conduct a systematic comparison focusing on three aspects: basic ground-state properties, shell structures, and superheavy nuclei.

The paper is organized as follows. The DRHFB theoretical framework with the PCF-PK1 functional and the

CPC Accepted

numerical details are described in Secs. **2** and **3**. The results are presented in Secs. **4** and 5. A summary is given in Sec. 6.

II. THEORETICAL FRAMEWORK

A. Relativistic Point-coupling Functional with Localized Exchange Terms

The ground states of finite nuclei are described within the axially deformed relativistic Hartree–Fock–Bogoliubov (RHFB) framework with the density-dependent point-coupling functional PCF-PK1 [47]. The starting point is an effective Lagrangian density comprising the free-nucleon, four-fermion point-coupling, derivative, and electromagnetic interaction terms [47, 51, 52],

$$\mathcal{L} = \mathcal{L}_{\text{free}} + \mathcal{L}_{\text{4f}} + \mathcal{L}_{\text{der}} + \mathcal{L}_{\text{em}}, \tag{1}$$

with

$$\mathcal{L}_{\text{free}} = \bar{\psi}(\mathrm{i}\gamma_\mu\partial^\mu - M)\psi, \tag{2a}$$

$$\mathcal{L}_{\text{4f}} = -\frac{1}{2}\sum_{i\in C}\alpha_i(\bar{\psi}\Gamma_i\psi)(\bar{\psi}\Gamma^i\psi), \tag{2b}$$

$$\mathcal{L}_{\text{der}} = -\frac{1}{2}\delta_S\partial_\mu(\bar{\psi}\psi)\partial^\mu(\bar{\psi}\psi), \tag{2c}$$

$$\mathcal{L}_{\text{em}} = -e\bar{\psi}\gamma_\mu\frac{1-\tau_3}{2}\psi A^\mu - \frac{1}{4}F_{\mu\nu}F^{\mu\nu}. \tag{2d}$$

Here, ψ denotes the nucleon field, M is the nucleon mass, α_i and δ_S are the coupling constants, A^μ is the electromagnetic field, and $F_{\mu\nu} = \partial_\mu A_\nu - \partial_\nu A_\mu$. The convention $\tau_3 = +1$ (-1) is adopted for neutrons (protons). The Lorentz–isospin channels are

$$C = \{S, tS, V, tV, T, tT, PS, tPS, PV, tPV\}, \tag{3}$$

where S, V, T, PS, and PV denote the scalar, vector, tensor, pseudoscalar, and pseudovector channels, respectively, and the prefix t denotes an isovector channel. The corresponding point-coupling vertices Γ_i are

$$\Gamma_i \in \{1, \vec{\tau}, \gamma_\mu, \gamma_\mu\vec{\tau}, \sigma_{\mu\nu}, \sigma_{\mu\nu}\vec{\tau}, \gamma_5, \gamma_5\vec{\tau}, \gamma_5\gamma_\mu, \gamma_5\gamma_\mu\vec{\tau}\}. \tag{4}$$

The Hamiltonian is obtained via a Legendre transformation, and the nucleon field is expanded in an arbitrary complete single-particle Dirac basis $\{\phi_l\}$ within the no-sea approximation [47],

$$\psi(\boldsymbol{r}) = \sum_k \phi_k(\boldsymbol{r})c_k, \qquad \psi^\dagger(\boldsymbol{r}) = \sum_k \phi_k^\dagger(\boldsymbol{r})c_k^\dagger, \tag{5}$$

where $c_k^\dagger$ and c_k respectively create and annihilate a nucleon in the basis state ϕ_k.

In the Hartree–Fock (HF) approximation, the nuclear ground state is represented by a single Slater determinant constructed from the A occupied single-particle states,

$$|\Phi_{\text{HF}}\rangle = \prod_{k=1}^{A} c_k^\dagger|-\rangle, \tag{6}$$

where $|-\rangle$ denotes the bare vacuum state. The expectation value of the Hamiltonian in this Slater determinant yields the mean-field energy.

$$\begin{aligned} E_{\text{MF}} &= \langle\Phi_{\text{HF}}|\hat{H}|\Phi_{\text{HF}}\rangle \\ &= E_{\text{kin}} + E_{\text{4f}} + E_{\text{der}} + E_{\text{em}}. \end{aligned} \tag{7}$$

The four-fermion term E_{4f} comprises Hartree and Fock contributions. The Fierz transformation is applied [46, 53−55]

$$[\bar{\phi}_k\Gamma_i\phi_l][\bar{\phi}_l\Gamma^i\phi_k] = \sum_j \Lambda_{ij}[\bar{\phi}_k\Gamma_j\phi_k][\bar{\phi}_l\Gamma^j\phi_l], \tag{8}$$

where Λ_{ij} is the Fierz matrix; thus, the Fock terms can be expressed as linear combinations of Hartree terms. For details, see Refs. [46, 47, 55]. The Coulomb exchange term is neglected in the PCF-PK1 parametrization.

The coupling strengths in the S, V, tS, and tV channels are density-dependent [47, 56],

$$\alpha_i(\rho_V) = \alpha_i(\rho_{\text{sat}})f_i(x), \tag{9}$$

$$f_i(x) = a_i\frac{1+b_i(x+d_i)^2}{1+c_i(x+d_i)^2}, \tag{10}$$

with $x = \rho_V/\rho_{\text{sat}}$, where ρ_V denotes the vector density and ρ_{sat} denotes the saturation density of symmetric nuclear matter. The coupling constants α_T and δ_S are density-independent.

B. Bogoliubov Transformation and RHFB Equation

For open-shell nuclei, pairing correlations play an essential role in determining ground-state properties. The Bogoliubov method provides a unified, self-consistent

CPC Accepted

treatment of the mean field in the particle–hole channel and the pairing field in the particle–particle channel [57]. The quasiparticle creation and annihilation operators are introduced through the transformation

$$\beta_k^\dagger = \sum_l \left(U_{lk} c_l^\dagger + V_{lk} c_l\right), \tag{11}$$

$$\beta_k = \sum_l \left(U_{lk}^* c_l + V_{lk}^* c_l^\dagger\right), \tag{12}$$

where the quasiparticle wave functions U and V are four-component Dirac spinors. The nuclear ground state $|\Phi\rangle$ is defined as the quasiparticle vacuum.

$$\beta_k|\Phi\rangle = 0 \qquad \text{for all } k. \tag{13}$$

The normal density matrix and the pairing tensor associated with this vacuum are

$$\rho_{ll'} = \langle\Phi|c_{l'}^\dagger c_l|\Phi\rangle = (V^* V^T)_{ll'}, \tag{14}$$

$$\kappa_{ll'} = \langle\Phi|c_{l'} c_l|\Phi\rangle = (V^* U^T)_{ll'}. \tag{15}$$

Within the RHFB framework, the quasiparticle wave functions are determined by self-consistently solving the Bogoliubov equation.

$$\begin{pmatrix} \hat{h} - \lambda_\tau & \hat{\Delta} \\ -\hat{\Delta}^* & -\hat{h}^* + \lambda_\tau \end{pmatrix} \begin{pmatrix} U_k \\ V_k \end{pmatrix} = E_k \begin{pmatrix} U_k \\ V_k \end{pmatrix}, \tag{16}$$

where E_k is the quasiparticle energy, λ_τ is the chemical potential for neutrons or protons, and the average particle numbers are constrained by $N_\tau = \mathrm{Tr}\rho_\tau$ for $\tau = n, p$.

Because the Fock terms of the point-coupling interaction have been localized through the Fierz transformation, the single-particle Hamiltonian retains the local Dirac form

$$\hat{h} = \boldsymbol{\alpha}\cdot\boldsymbol{p} + \beta[M + S] + V^0 - \mathrm{i}\beta\boldsymbol{\alpha}\cdot\boldsymbol{T}^0. \tag{17}$$

The scalar, vector, and tensor potentials are expressed as

$$S = \alpha_S\rho_S + \alpha_{tS}\tau_3\rho_{tS} + \delta_S\Delta\rho_S, \tag{18a}$$

$$V^0 = \alpha_V\rho_V + \alpha_{tV}\tau_3\rho_{tV} + e\frac{1-\tau_3}{2}A^0 + \Sigma_R^0, \tag{18b}$$

$$\boldsymbol{T}^0 = 2\alpha_T\boldsymbol{j}_T^0 + 2\alpha_{tT}\tau_3\boldsymbol{j}_{tT}^0. \tag{18c}$$

Σ_R^0 denotes the rearrangement self-energy associated with the density-dependent couplings [47, 58, 59]. The corresponding local densities and currents are defined as

$$\rho_S = \sum_{k>0}\bar{V}_k V_k, \quad \rho_{tS} = \sum_{k>0}\bar{V}_k\tau_3 V_k, \tag{19a}$$

$$\rho_V = \sum_{k>0}\bar{V}_k\gamma^0 V_k, \quad \rho_{tV} = \sum_{k>0}\bar{V}_k\gamma^0\tau_3 V_k, \tag{19b}$$

$$\boldsymbol{j}_T^0 = \sum_{k>0}\bar{V}_k\mathrm{i}\gamma^0\boldsymbol{\gamma}V_k, \quad \boldsymbol{j}_{tT}^0 = \sum_{k>0}\bar{V}_k\mathrm{i}\gamma^0\boldsymbol{\gamma}\tau_3 V_k. \tag{19c}$$

For the time-reversal-invariant system considered here, the time-odd spatial vector currents and the σ^{ij} component of the tensor channel vanish. The pseudoscalar density and pseudovector current also do not contribute to parity-conserving ground states.

The pairing field is generated by a translationally invariant, finite-range separable interaction [60],

$$\begin{aligned} V^{pp}(\boldsymbol{r}_1, \boldsymbol{r}_2, \boldsymbol{r}_1', \boldsymbol{r}_2') = &-G\delta(\boldsymbol{R} - \boldsymbol{R}')P(\boldsymbol{r})P(\boldsymbol{r}') \\ &\times\tfrac{1}{2}(1 - P^\sigma), \end{aligned} \tag{20}$$

where $\boldsymbol{R} = (\boldsymbol{r}_1 + \boldsymbol{r}_2)/2$, $\boldsymbol{r} = \boldsymbol{r}_1 - \boldsymbol{r}_2$, and

$$P(\boldsymbol{r}) = \frac{1}{(4\pi a^2)^{3/2}}\exp\left(-\frac{r^2}{4a^2}\right). \tag{21}$$

The operator $(1 - P^\sigma)/2$ projects onto the spin-singlet channel. The pairing field and pairing energy are then calculated as

$$\hat{\Delta}_{ab} = \frac{1}{2}\sum_{cd}\langle ab|V^{pp}|cd\rangle\kappa_{cd}, \tag{22}$$

$$E_{\mathrm{pair}} = \frac{1}{4}\sum_{abcd}\kappa_{ab}^*\langle ab|V^{pp}|cd\rangle\kappa_{cd} = \frac{1}{2}\sum_{ab}\kappa_{ab}^*\hat{\Delta}_{ab}. \tag{23}$$

The finite range of the interaction provides a natural ultraviolet regularization, and the matrix elements in a harmonic-oscillator basis reduce to a finite sum of separable terms [60, 61].

To solve Eq. (17) for axially deformed nuclei, axial and reflection symmetries are imposed [61−64]. The quasiparticle states can therefore be classified by (Ω, π, τ), which denote the angular-momentum projection, parity,

CPC Accepted

and isospin, respectively. The RHFB equation is diagonalized independently in each symmetry block. For definiteness, we present the expansion of the four-component Dirac spinor V_k; the expansion of U_k is completely analogous:

$$V_k(\boldsymbol{r},s)=\begin{pmatrix}F_{V,k}(\boldsymbol{r},s)\\ \mathrm{i}G_{V,k}(\boldsymbol{r},s)\end{pmatrix}. \tag{24}$$

The upper and lower components are expanded separately in their corresponding axially deformed harmonic-oscillator subspaces,

$$F_{V,k}(\boldsymbol{r},s)=\sum_{\alpha}f_{\alpha k}^{(V)}\Phi_{\alpha}(\boldsymbol{r},s), \tag{25}$$

$$G_{V,k}(\boldsymbol{r},s)=\sum_{\tilde{\alpha}}g_{\tilde{\alpha}k}^{(V)}\Phi_{\tilde{\alpha}}(\boldsymbol{r},s). \tag{26}$$

Here, α and $\tilde{\alpha}$ label the oscillator states associated with the upper and lower components, respectively. The basis states are given by [61, 62]

$$\Phi_{\alpha}(\boldsymbol{r},s)=\phi_{n_z}(z)\phi_{n_\perp}^{|m_l|}(r_\perp)\frac{e^{\mathrm{i}m_l\varphi}}{\sqrt{2\pi}}\chi_{m_s}(s), \tag{27}$$

in cylindrical coordinates $\boldsymbol{r}=(r_\perp,\varphi,z)$, where $\alpha=\{n_z,n_\perp,m_l,m_s\}$. The corresponding major-shell quantum numbers are

$$N=n_z+2n_\perp+|m_l|. \tag{28}$$

The state $\Phi_{\tilde{\alpha}}$ is defined analogously, where $\tilde{\alpha}=\{\tilde{n}_z,\tilde{n}_\perp,\tilde{m}_l,\tilde{m}_s\}$. For a quasiparticle state characterized by the quantum numbers (Ω,π), the two subspaces are selected according to

$$m_l+m_s=\tilde{m}_l+\tilde{m}_s=\Omega, \tag{29}$$

$$(-1)^N=\pi,\qquad (-1)^{\widetilde{N}}=-\pi. \tag{30}$$

Thus, the upper and lower oscillator components have the same angular-momentum projection but opposite orbital parities, as required for a Dirac spinor with definite parity. After each diagonalization, the densities and fields are reconstructed from the quasiparticle wave functions, and Eq. (17) is iterated until self-consistency is achieved.

The axial quadrupole deformation is characterized by the dimensionless mass quadrupole deformation parameter

$$\beta_2=\frac{\sqrt{5\pi}}{3AR_0^2}Q_{20}, \tag{31}$$

where A denotes the mass number, $R_0=1.2A^{1/3}\,\mathrm{fm}$, and Q_{20} denotes the quadrupole moment.

$$Q_{20}=\int d^3r\rho_V(\boldsymbol{r})\left(2z^2-x^2-y^2\right). \tag{32}$$

C. Total Energy

After the RHFB equations are solved self-consistently, the RHFB energy is evaluated in terms of the quasiparticle wave functions and local densities as

$$E_{\mathrm{RHFB}}=E_{\mathrm{kin}}+E_{\mathrm{4f}}+E_{\mathrm{der}}+E_{\mathrm{em}}+E_{\mathrm{pair}}. \tag{33}$$

The individual particle–hole contributions are

$$E_{\mathrm{kin}}=\int d^3r\sum_{k>0}V_k^{\dagger}\left(-\mathrm{i}\boldsymbol{\alpha}\cdot\nabla+\beta M\right)V_k, \tag{34a}$$

$$E_{\mathrm{4f}}=\frac{1}{2}\int d^3r\left[\alpha_S\rho_S^2+\alpha_{tS}\rho_{tS}^2+\alpha_V\rho_V^2+\alpha_{tV}\rho_{tV}^2-2\alpha_T\boldsymbol{j}_T^0\cdot\boldsymbol{j}_T^0-2\alpha_{tT}\boldsymbol{j}_{tT}^0\cdot\boldsymbol{j}_{tT}^0\right], \tag{34b}$$

$$E_{\mathrm{der}}=-\frac{1}{2}\delta_S\int d^3r[\nabla\rho_S(\boldsymbol{r})]^2, \tag{34c}$$

$$E_{\mathrm{em}}=\frac{1}{2}e\int d^3r\rho_p(\boldsymbol{r})A^0(\boldsymbol{r}). \tag{34d}$$

Here, $\rho_p=(\rho_V-\rho_{tV})/2$ is the proton density. The Fock contributions are already included in the couplings α_i after the Fierz transformation. The pairing contribution E_{pair} is given in Eq. (24).

Following Ref. [65], the breaking of translational invariance is corrected microscopically by

$$E_{\mathrm{c.m.}}=-\frac{\langle\boldsymbol{P}_{\mathrm{c.m.}}^2\rangle}{2MA},\qquad \boldsymbol{P}_{\mathrm{c.m.}}=\sum_{i=1}^{A}\boldsymbol{p}_i. \tag{35}$$

where $\boldsymbol{P}_{\mathrm{c.m.}}$ denotes the total momentum in the center-of-mass (c.m.) frame. For a deformed intrinsic state, the energy gained by restoring rotational symmetry is estimated using the cranking approximation [66],

$$E_{\mathrm{rot}}=-\frac{\langle\hat{\boldsymbol{J}}^2\rangle}{2\mathcal{I}_{\mathrm{IB}}}, \tag{36}$$

CPC Accepted

where $\mathcal{I}_{\rm IB}$ is the Inglis–Belyaev moment of inertia [57]. For weakly deformed nuclei with $|\beta_2| < 0.05$, $E_{\rm rot}$ is set to zero. Finally, the total corrected ground-state energy is given by

$$E_{\rm tot} = E_{\rm RHFB} + E_{\rm c.m.} + E_{\rm rot}. \tag{37}$$

For odd-A and odd–odd nuclei, we adopt the equal filling approximation (EFA) [39, 67, 68] to simplify the calculations. This approximation preserves time-reversal symmetry by averaging equally over a blocked single-particle state and its time-reversed partner.

III. NUMERICAL DETAILS

For the particle-particle channel, we employ a finite-range separable force with strength $G = 657.5419$ MeV fm^3 and width $a = 0.644$ fm [47]. The localized RHFB equation is solved in a basis of harmonic-oscillator wave functions [61].

To determine an appropriate number of major shells $N_{\rm f}$, Fig. 1 shows the total energies of ^{24}Ne, ^{160}Nd, and ^{250}U as functions of $N_{\rm f}$, with all energies shifted relative to the reference value at $E(N_{\rm f} = 32)$. The yellow shaded band indicates deviations within 0.025 MeV of the reference value. The quadrupole deformation values β_2 as functions of $N_{\rm f}$ are indicated by red circles.

For all three nuclei, the quadrupole deformation β_2 remains essentially unchanged in the range $N_{\rm f} = 16$ to 32. For the light nucleus ^{24}Ne, the variation in the total energy is very small, generally within 0.05 MeV, and the error is less than 0.025 MeV when $N_{\rm f} \geq 22$. For the medium-heavy nucleus ^{160}Nd, an $N_{\rm f}$ of at least 28 is required to reduce the error to less than 0.025 MeV. For the heavy nucleus ^{250}U, the same precision requires $N_{\rm f} = 30$. Accordingly, we adopt $N_{\rm f} = 22$, 28, and 30 for nuclei with $Z \leq 28$, $28 < Z \leq 82$, and $Z > 82$, respectively.

Using an even-Z, even-N (hereafter even-even) nucleus with neutron number N and proton number Z as a reference, the odd-A nucleus $(N+1, Z)$ is obtained by adding a neutron. For such odd-A nuclei, the configuration corresponding to the lowest neutron quasiparticle energy is blocked during the iterative calculation, from which the final ground state is determined. Similarly, for the odd-odd nucleus $(N+1, Z+1)$, the configurations corresponding to the lowest neutron and proton quasiparticle energies are blocked simultaneously.

To locate the correct energy minimum, it is reliable to examine the potential energy curve (PEC). In this work, the PECs of even-even nuclei are calculated. The results of unconstrained calculations for even-even nuclei are compared with their corresponding PECs, while the results for odd-A and odd-odd nuclei are compared with the PECs of neighboring even-even nuclei. This procedure ensures that the correct ground state is identified for each nucleus through unconstrained calculations.

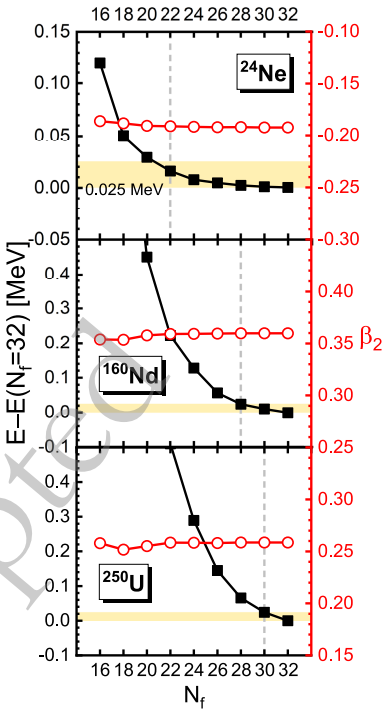

Fig. 1. (color online) The total energies of ^{24}Ne, ^{160}Nd, and ^{250}U as functions of the number of major shells $N_{\rm f}$, with all energies shifted relative to the reference point $N_{\rm f} = 32$, are shown by black squares. The yellow shaded band indicates the interval within an error of 0.025 MeV from the reference point. The quadrupole deformation as a function of $N_{\rm f}$ is shown by red circles. The grey dashed lines mark the finally chosen $N_{\rm f}$.

IV. RESULTS AND DISCUSSIONS

A. Basic Properties

1. *Deformations, Binding Energies, and Drip Lines*

Within the localized DRHFB theory, systematic calculations of nuclei with $8 \leq Z \leq 120$ are performed using the PCF-PK1 functional. Figure 2 shows the quadrupole deformation parameter β_2 for all nuclei; the magic numbers are indicated by grey dashed lines.

In this work, nuclei are considered bound only if their separation energies are positive and their Fermi energies are negative. According to this criterion, 7550 nuclei are bound in the calculation without $E_{\rm rot}$, whereas 7348 nuclei are bound when $E_{\rm rot}$ is included. Among the 7550 nuclei predicted to be bound, 818 are identified as spherical ($|\beta_2| < 0.001$), 5350 as prolate, and 1382 as oblate. Nuclei in the vicinity of magic numbers are generally spherical, whereas those in mid-shell regions are well deformed, as

CPC Accepted

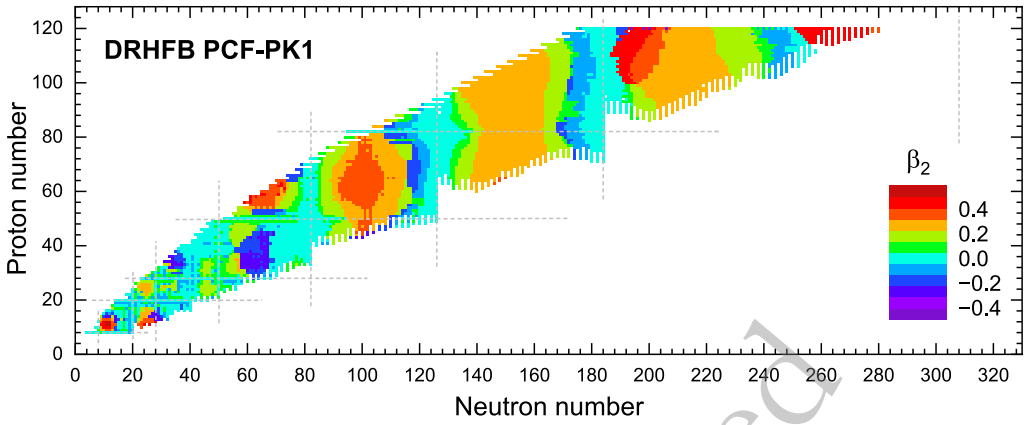

Fig. 2. (color online) The quadrupole deformation parameter β_2 calculated by DRHFB theory using functional PCF-PK1. Magic numbers are shown by grey dashed lines.

expected. The deformation parameter generally follows a parabolic trend along an isotopic chain between two major shell closures. This feature, which was also found in the RMF+BCS calculation with TMA [32] and in DRHBc calculations with PC-PK1 [40, 41], is clearly visible, for example, in the isotopic chains between $N = 82$ and 126. Nuclei in isotopic chains with magic proton numbers are usually deformed in the mid-shell region, e.g., $Z = 50$. In contrast, those in the entire isotonic chain with a magic neutron number remain spherical, e.g., $N = 82$. This feature indicates that neutron shell gaps have a more pronounced effect on nuclear deformations, which can also be found in other CDFT calculations [34]. In the light-mass region, neutron-rich nuclei with $N = 28$ deviate from spherical shapes, indicating the weakening of magicity in regions far from the β-stability line.

A clear competition between prolate and oblate shapes appears around $(Z = 40, N = 60)$ and $(Z = 70, N = 116)$, suggesting shape coexistence and the possible relevance of triaxial deformation, as predicted in the triaxial RHB calculations with PC-PK1 [42]. Similar shape competition has also been identified in light nuclei, such as around ^{42}Al, where triaxial deformations have been predicted by the triaxial relativistic Hartree-Bogoliubov theory in continuum (TRHBc) [69, 70]. These nuclei are difficult to describe precisely at the mean-field level [71], and correlations beyond the mean field are expected to be taken into account [72, 73]. In addition, there is a dramatic change from spherical to strongly prolate shapes in the superheavy-nucleus region, e.g., after the shell closure at $N = 184$, which is related to sudden changes in binding energies and radii.

Taking deformation into account, the 7550 bound nuclei are represented by open squares in Fig. 3, and the colored squares indicate the relative deviation of the binding energies, with $E_{\rm rot}$ included, from the experimental values [9].

For most nuclei, the relative deviations between theory and experiment are within 0.5%. In mid-shell regions, the binding energies are slightly underestimated, whereas near magic numbers, such as in neutron-rich nuclei around $N = 50, 82$ and the isotonic chain with $N = 126$, they are slightly overestimated. In addition, the overestimation of binding energies for neutron-rich nuclei near $N = 20$ and 40 is also observed in other predictions, suggesting that the underlying physical mechanism remains unclear.

Comparisons of the available binding energies, separation energies, and drip lines are shown in Table 1. The other models listed in this table include the DRHBc calculations with PC-PK1 and the RMF+BCS calculations with TMA, for which the contributions of rotational correction energies are indicated separately. Rotational corrections are not explicitly included in the TMA calculations; however, some effects associated with rotational corrections have been absorbed phenomenologically into the parameterization.

For even-Z nuclei, when the rotational correction energy $E_{\rm rot}$ is excluded, the rms deviation of PCF-PK1 with respect to 1247 data points is 2.883 MeV, which is 0.3 MeV higher than that of PC-PK1 and 0.8 MeV higher than that of TMA. When the rotational correction energy is included, PCF-PK1 yields an rms deviation of 1.734 MeV, which remains 0.3 MeV higher than that of PC-PK1 but is lower than that of TMA.

To identify a major source of the difference in rms deviations between PCF-PK1 and PC-PK1, we examine even-even nuclei. We find 62 nuclei for which PCF-PK1 predicts a spherical ground state whereas PC-PK1 predicts a deformed one. Most of these nuclei exhibit soft potential-energy surfaces or competing minima in the PC-PK1 calculations [42, 77]. With rotational corrections included, the rms deviations for this subset are 2.96 MeV for PCF-PK1 and 1.00 MeV for PC-PK1. For the remaining even-even nuclei, the corresponding deviations are nearly identical, at 1.52 and 1.56 MeV, respectively. The deformed PC-PK1 solutions gain additional binding from rotational corrections, whereas these corrections are not

CPC Accepted

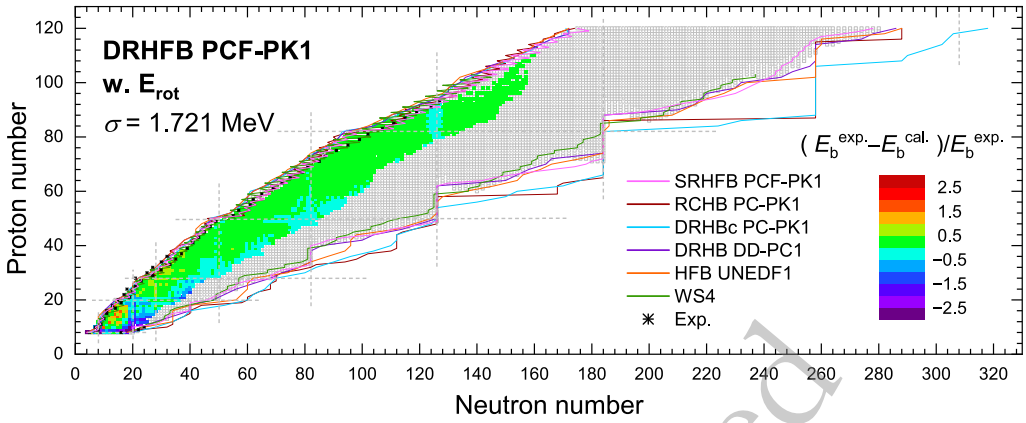

Fig. 3. (color online) A total of 7550 bound nuclei with $8 \le Z \le 120$ derived from the theoretical calculations are represented by open squares. The relative deviations of the binding energies (with rotational correction energy included) from the experimental values [9] are shown by colored squares. For comparison, the drip line positions predicted by other models are also displayed, including PCF-PK1 under the spherical approximation, PC-PK1 [26, 40, 41], DD-PC1 [33, 34], UNEDF1 [17], and WS4 [11]. Experimentally confirmed drip lines [74−76] are marked by snowflake symbols. Magic numbers are indicated by grey dashed lines.

Table 1. The rms deviations of the calculated binding energies and separation energies from AME2020 [9], in units of MeV, as well as the rms deviations of the theoretically predicted neutron (σ_n^{drip}) and proton (σ_p^{drip}) drip line positions from experimental data [74−76]. For binding energy and separation energies, the present works [DRHFB (PCF-PK1)], including results with and without E_{rot}, are compared with RMF+BCS (TMA) without E_{rot} [32]. In order to compare with DRHBc (PC-PK1) results with and without E_{rot}, results for nuclei with even-Z number are listed separately. For drip lines, the present work of DRHFB (PCF-PK1) calculation denoted as PCF-PK1(D), is compared with the spherical RHFB (PCF-PK1) denoted as PCF-PK1(S) [50], RMF+BCS (TMA) [32], DRHBc(PC-PK1) [41], and RHB (DD-PC1) [34]. It is noticed that DRHBc(PC-PK1) and RHB (DD-PC1) results include only even-*Z* nuclei and even-even nuclei, respectively.

		$\sigma(E_b)$	$\sigma(S_{2n})$	$\sigma(S_{2p})$	$\sigma(S_n)$	$\sigma(S_p)$
Even-*Z*	DRHFB$^{w.o.rot}$	2.883	0.913	0.779	0.660	-
	DRHFB$^{w.rot}$	1.734	1.008	0.924	0.946	-
	DRHBc$^{w.o.rot}$	2.562	0.953	0.929	0.749	-
	DRHBc$^{w.rot}$	1.433	0.989	1.046	0.774	-
	RMF+BCS	2.076	1.349	1.169	0.731	-
All	DRHFB$^{w.o.rot}$	2.882	0.885	0.776	0.606	0.598
	DRHFB$^{w.rot}$	1.721	0.981	1.030	0.896	1.034
	RMF+BCS	2.118	1.443	1.219	0.660	0.828
		PCF-PK1(D)	PCF-PK1(S)	TMA	PC-PK1	DD-PC1
Drip line	σ_n^{drip}	2.65	3.46	2.58	4.00	2.83
	σ_p^{drip}	1.18	2.02	2.77	1.04	1.04

considered for the spherical PCF-PK1 solutions. These results identify differences in predicted ground-state shapes and the associated treatment of collective correlations as a major source of the difference in accuracy. A more complete description of quadrupole collective correlations using a five-dimensional collective Hamiltonian (5DCH) [72, 78] or the generator coordinate method (GCM) [79, 80] is therefore needed for these nuclei.

For all nuclei, experimental data are available for 2373 nuclei, including 635 even-even nuclei, 612 even-odd nuclei, 574 odd-even nuclei, and 552 odd-odd nuclei. The corresponding rms deviations without rotational energy corrections are 2.995 MeV, 2.766 MeV, 2.883 MeV, and 2.872 MeV, respectively, and the total rms deviation is 2.882 MeV. The PCF-PK1 result remains approximately 0.8 MeV higher than that of TMA. When E_{rot} is included, the rms deviation decreases to 1.721 MeV, representing a substantial improvement over the TMA results. Compared with the rms deviation of 7.170 MeV [50] obtained under the spherical approximation with the same

CPC Accepted

model, the descriptive accuracy is greatly improved. In particular, the systematic underestimation in regions with noticeable deformations, such as $(Z\sim60, N\sim100)$, $(Z\sim100, N\sim150)$, proton-rich nuclei with $Z>20$, and some light nuclei with $Z<20$ and $N<20$, as shown in Fig. 2, is improved. In addition, the rms deviation of the binding energies for even-Z nuclei differs only slightly from that for all nuclei, indicating the stability of the theoretical calculations for even and odd nuclei.

For separation energies, the rms deviations are consistently lower than those obtained with PC-PK1 and TMA when $E_{\rm rot}$ is excluded. For instance, among even-Z nuclei, $\sigma(S_{2\rm p})$ obtained with PCF-PK1 is noticeably lower than that of TMA by approximately 0.4 MeV and is approximately 0.15 MeV smaller than that of PC-PK1. After $E_{\rm rot}$ is included, the rms deviations of the separation energies increase in both the PCF-PK1 and PC-PK1 calculations. Thus, $E_{\rm rot}$ improves the accuracy of the mass description but consistently worsens the description of separation energies, especially for $S_{\rm n}$ and $S_{\rm p}$. This may be related to the use of the cranking approximation to evaluate $E_{\rm rot}$, which is not well suited for weakly deformed nuclei.

When deformation is considered, the 7210 bound nuclei predicted under the spherical approximation increase to 7550, and the drip-line positions change accordingly. As shown in Table 1, the predictions of PCF-PK1 for both the neutron and proton drip-line positions are generally improved compared with the spherical case. Compared with other models, the neutron drip line obtained by PCF-PK1 is close to those of TMA and DD-PC1 and is smaller than that of PC-PK1. With continuum effects included, PC-PK1 predicts more extended neutron drip lines than the other calculations, as shown in Fig. 3. Experimentally, the neutron drip line has now reached the Ne ($Z=10$) isotopes [76], where the PCF-PK1 prediction differs from experiment by only one neutron, whereas the PC-PK1 prediction extends by four neutrons, supporting the smaller deviation in the PCF-PK1 results.

Because of Coulomb-barrier effects, the proton drip lines predicted by different models are close to the valley of stability, and the discrepancies are small. For the proton drip line, the PCF-PK1 results are significantly closer to the experimental data than those of TMA. When all nuclei are included, the rms deviation of PCF-PK1 is only slightly higher than those of PC-PK1 and DD-PC1, for which only even-Z and even-even nuclei are considered, respectively. For even-Z and even-even nuclei, the rms deviations of PCF-PK1 are 1.32 and 1.94, respectively, which are higher than the PC-PK1 and DD-PC1 results. In addition, a phenomenon arising from the interplay between odd-even effects and deformation effects appears in the PCF-PK1 predictions, eventually forming the so-called "peninsula" beyond the drip line [81−84], for example near $(Z=64, N=138)$ and $(Z=92, N=200)$, as shown in Fig. 3.

2. *Charge Radii*

The nuclear charge radius is another fundamental ground-state observable, and deformation effects play a crucial role in its description [85]. Fig. 4 displays the deviations of the calculated charge radii from the experimental values [86, 87]. The axially deformed results, shown as orange stars, are compared with the spherical results, shown as blue circles. The light blue and dark blue shaded bands indicate deviations within 0.05 fm and 0.03 fm, respectively.

With deformation included, the rms deviations for 620 even-Z and 390 odd-Z nuclei are 0.0267 fm and 0.0341 fm, respectively, yielding a total rms deviation of 0.0298 fm. This represents a noticeable improvement over the spherical result of 0.0362 fm [50], as expected. Compared with the DRHBc calculation using the PC-PK1 interaction, which gives an rms deviation of 0.033 fm for 620 even-Z nuclei [41], the accuracy is improved by about 19% in the present work. Among the 1010 data points, 90.20% and 77.82% of the total lie within 0.05 fm and 0.03 fm, respectively.

For light nuclei, the inclusion of deformation introduces only minor changes in the charge radii. In the mid-shell region between $N=50$ and 82, the significant overestimation of charge radii is reduced compared with the spherical results, and these nuclei exhibit noticeable deformations, as shown in Fig. 2. Among these nuclei, for those with $Z=54$-56 and $N\approx66$, although the accuracy is improved, the predicted charge radii change from being underestimated to overestimated.

In the mid-shell region between $N=82$ and 126, the rms deviation for the Lu ($Z=71$) isotopic chain is 0.1007 fm for spherical nuclei and is reduced to 0.0207 fm when deformation is included, representing the most notable improvement in charge radii across the nuclear chart. For

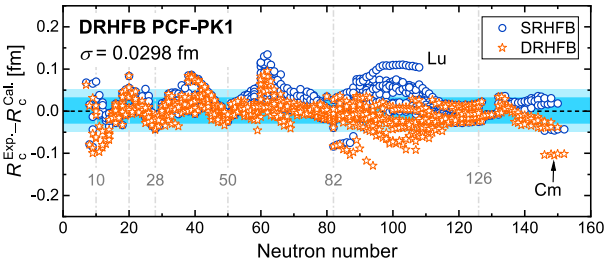

Fig. 4. (color online) The deviations of the theoretical charge radii from the 1010 experimental values [86, 87], calculated by DRHFB model (orange stars), and by RHFB model under the spherical approximation (blue circles), using PCF-PK1 interaction. Light blue and dark blue shaded bands indicate the deviations of ±0.05 fm, and ±0.03 fm, respectively. Grey dashed lines represent the magic numbers $N=20,28,50,82,126$.

CPC Accepted

the $Z = 72$-76 isotopes, the predicted charge radii change from being underestimated to overestimated; the accuracy is improved for $Z = 72,73$ but becomes worse for $Z = 74$-76. The discrepancies are more pronounced for some Pt ($Z = 78$) and Hg ($Z = 80$) isotopes around $N = 104$, for which the predicted deformation parameter $|\beta_2| \approx 0.3$ is inconsistent with the experimental value ($|\beta_2| < 0.2$) [88]. Recent studies of Hg isotopes have also emphasized the important role of deformation in the evolution of nuclear charge radii [89].

For nuclei with neutron number $N > 126$, the inclusion of deformation worsens the description of charge radii for $Z = 92,94,95$ and N around 140, changing them from slight underestimates to overestimates. The discrepancies increase to about 0.1 fm for Cm ($Z = 96$) isotopes around $N = 150$, as indicated in Fig. 4. Similar discrepancies have also been found in other CDFT [34, 41] and nonrelativistic calculations [90]. These calculations show that the charge radii of Cm follow the increasing trend with proton number for a fixed neutron number. However, experimentally, the charge radii of Cm isotopes are smaller than those of U ($Z = 92$) and Pu ($Z = 94$) isotopes, giving rise to the unusual behavior of the charge radii of U–Pu–Cm isotopes. This experimental phenomenon is not reproduced by current CDFT calculations.

3. *α-decay Energies*

The α-decay energy, Q_α, serves as a sensitive probe of shell structure, and the theoretical Q_α value can be extracted from binding energies.

$$Q_\alpha(Z,N) = E_{\rm b}(Z-2,N-2) + E_{\rm b}(2,2) - E_{\rm b}(Z,N). \quad (38)$$

To illustrate this, Fig. 5 shows the deviations of Q_α from the experimental values [9] for nuclei with $Q_\alpha > 0$; the upper and lower panels show the results without and with rotational-energy corrections, respectively.

Without $E_{\rm rot}$, the rms deviation for the 1079 data points is 0.7215 MeV. This represents a noticeable improvement over the spherical result (1.6263 MeV) obtained with the same functional [50], suggesting that deformation effects play a vital role in the description of Q_α. Around $N = 82$ and 126, relatively large discrepancies are observed in the upper panel. These discrepancies arise from the overestimation of binding energies at the shell closures $N = 82$ and 126 and the underestimation of those for neighboring nuclei.

Incorporating the contribution of $E_{\rm rot}$ slightly increases the rms deviation to 0.7511 MeV compared with the result without $E_{\rm rot}$. Regardless of whether rotational corrections are included, the present work provides a better description than the RMF+BCS results with TMA ($\sigma = 1.115$ MeV for the entire nuclear chart) [32], the

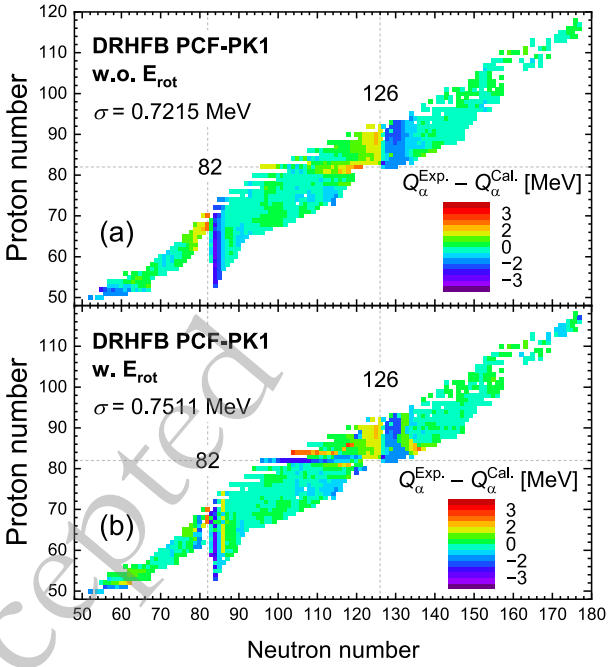

Fig. 5. (color online) Deviation of the calculated Q_α from the experiment [9] for nuclei with $Q_\alpha > 0$. The deformed calculations without rotational correction energy $E_{\rm rot}$ are plotted in the upper panel (a), and the results including $E_{\rm rot}$ are plotted in the lower panel (b). Magic numbers are shown by grey lines.

DRHBc results with PC-PK1 ($\sigma = 0.802$ MeV for even-Z nuclei) [41], and the DRHB result with DD-PC1 ($\sigma = 0.901$ MeV for even-even nuclei) [34]. Moreover, as shown in the lower panel, the description of Q_α for nuclei around $Z = 82$ becomes less satisfactory than that obtained without $E_{\rm rot}$. This is because the cranking approximation is not reliable for nearly spherical nuclei, leading to large discrepancies. Triaxial RHB calculations with PC-PK1 [42] have demonstrated that including beyond-mean-field correlations from the collective Hamiltonian method reduces the rms deviation of Q_α from 0.989 MeV to 0.552 MeV. This approach is applicable to both spherical and deformed nuclei and could be adopted in future work for further improvement.

B. Shell Structures

Shell gaps can serve as indicators of shell closures and are extracted from the second derivative of nuclear binding energies, taking the neutron case as an example.

$$S_{2n}(N,Z) = E_{\rm b}(N,Z) - E_{\rm b}(N-2,Z), \quad (39)$$

$$\delta_{2n}(N,Z) = S_{2n}(N,Z) - S_{2n}(N+2,Z), \quad (40)$$

where S_{2n} denotes the two-neutron separation energy,

CPC Accepted

and δ_{2n} denotes the neutron shell gap. Using the definitions above, Fig. 6 shows the two-neutron and two-proton shell gaps calculated using the DRHFB theory with PCF-PK1.

For the neutron shell gaps, peaks appear at the traditional magic numbers $N = 8$, 20, 50, 82, and 126, as well as at the predicted magic number $N = 184$. The peaks become smaller with increasing neutron number, suggesting a weakened shell effect in heavy nuclei. At the traditional magic number $N = 28$, however, PCF-PK1 does not yield a pronounced shell gap. The shell gaps at $N = 50$, 82, and 126 decrease near the neutron drip line, and this reduction is particularly pronounced for $N = 28$, suggesting the quenching or even collapse of traditional neutron magic numbers in neutron-rich nuclei. There are also indications of spherical or deformed subshells, such as $N = 14$ around $(Z = 14, N = 14)$, $N = 40$ in the $Z \approx 20$ region, and $N = 162$ around $Z = 110$. In the superheavy nucleus region, some isolated peaks around $(Z = 116, N = 190)$ are associated with the dramatic change in nuclear deformation from one nucleus to another.

For protons, peaks appear at the traditional magic numbers $Z = 8$, 20, 28, 50, and 82. As in the neutron case, the proton shell gaps become smaller with increasing proton number. The shell gaps at $Z = 28$ are weakened for neutron-rich nuclei around the drip line. In addition, the shell gaps exhibit no peak in the mid-shell regions around $(Z = 50, N = 110)$ and $(Z = 82, N = 160)$, where nuclear deformation is more pronounced, as shown in Fig. 2, indicating that shell gaps are influenced by deformation effects. There are also some peaks around $(Z = 12, N = 12)$, $(Z = 14, N = 14)$, and $(Z = 40, N = 40)$, suggesting the existence of deformed or spherical subshells in these regions. Furthermore, in the DRHFB calculations with PCF-PK1, no peaks appear at $Z = 58$ and 92, which is consistent with the removal of the spurious shells in the previous work [50].

The rms deviations of the two-neutron and two-proton shell gaps from experiment are 0.9986 and 0.8880 MeV, respectively, representing improvements of 0.1 and 0.25 MeV, respectively, over the spherical results. To specifically analyze the influence of deformation effects on the description of the shell gaps, Fig. 7 displays the relative differences in the two-nucleon shell gaps between the deformed and spherical calculations.

For the neutron shell gaps, the differences are less pronounced at magic numbers, as expected, since these nuclei remain spherical. Large discrepancies are concentrated in the mid-shell regions, e.g., around $N = 66$, 100,150, and 210, where the nuclear shapes deviate substantially from spherical symmetry. The notable increase at $N = 162$ suggests a possible deformed magic number, and the deformed superheavy doubly magic nucleus ^{270}Hs is discussed in Sec. 4.3. In the light-nucleus region, the

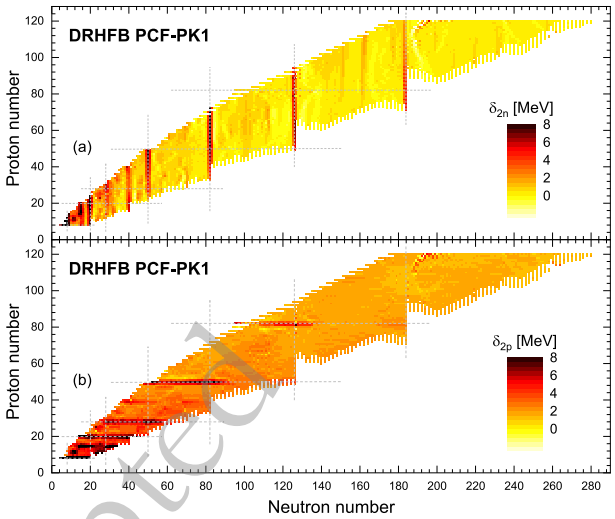

Fig. 6. (color online) Two-neutron (a) and two-proton (b) shell gaps obtained by DRHFB with PCF-PK1 are scaled by colors. Magic numbers are shown by grey dashed lines.

shell gaps are enhanced for nuclei with $Z = 12$ and $N = 12, 25$, $Z = 25$ and $N = 24, 46$, and $Z = 32$ and $N = 34, 46$. In contrast, the shell gaps are reduced around $N = 84$ and 120 for $Z = 50$-70, and around $N = 166$ for $Z = 82$-114, where the deformation effects are relatively weaker than those in the mid-shell regions. Moreover, the shell gaps are also reduced in the light-nucleus region, such as in neutron-rich nuclei around $N = 15$, 43, and 69.

For proton shell gaps, the differences between deformed and spherical results vanish for nuclei around doubly magic numbers. In the light-mass region, the proton shell gaps are significantly enhanced by deformation effects for nuclei around (12, 12), (12, 26), and (24, 24). In the mid-shell region, the proton shell gaps are enhanced in mass regions such as $(Z = 34, N = 60)$, $(Z = 70, N = 110)$, and $(Z = 108, N = 160)$, where the nuclear shapes deviate from spherical symmetry. In contrast, the proton shell gaps are significantly reduced for mid-shell nuclei with proton magic numbers, e.g., $(Z = 50, N = 100)$ and $(Z = 82, N = 160)$, indicating that deformation effects play a vital role in shell gaps. In addition, as discussed in Fig. 6, the shell gaps of nuclei near $N = 190$ in the superheavy-nucleus region show isolated peaks, consistent with the abrupt changes in the shell-gap difference between deformed and spherical results after the closed shell $N = 184$, as shown in Fig. 7.

To discuss the removal of the spurious shells from a more microscopic perspective, Fig. 8 displays the deviations of two-proton shell gaps from experimental values for Ce ($Z = 58$) and U ($Z = 92$) isotopes. The calculations include spherical (open red stars) [50] and deformed RHFB (solid red stars) results with PCF-PK1, spherical RCHB (open green triangles) [26] and DRHBc results with PC-PK1 (solid green triangles) [41], as well as spherical RHB (open blue circles) and DRHB results with

CPC Accepted

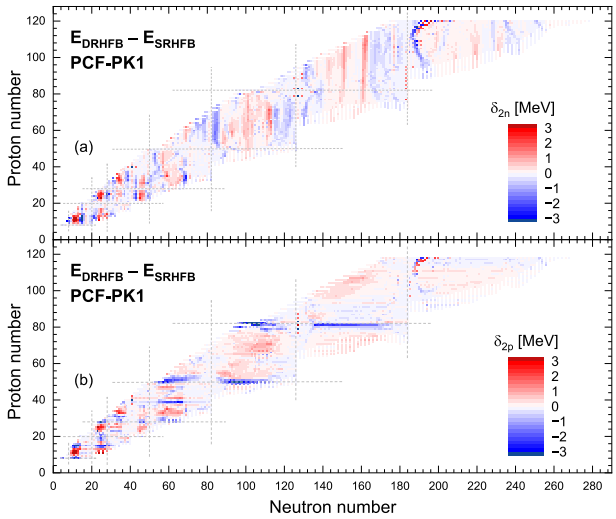

Fig. 7. (color online) The differences of two-neutron (a) and two-proton (b) shell gaps between axially deformed (DRHFB) and spherical calculations (SRHFB) with interaction PCF-PK1 are scaled by colors. Magic numbers are shown by grey dashed lines.

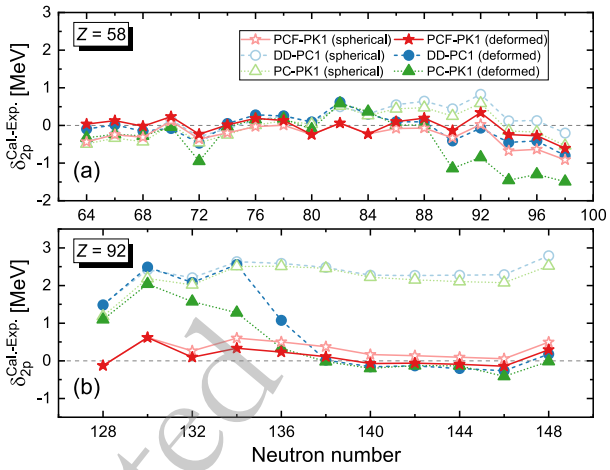

Fig. 8. (color online) Deviations of calculated two-proton shell gaps with respect to the experiment. The upper panel shows Ce isotopes (a), and the lower panel shows U isotopes (b). The spherical [50] and deformed calculations using PCF-PK1 (red stars), PC-PK1[26, 41] (green triangles), and DD-PC1 [34] (blue circles) are presented, where the spherical and deformed results are donated by open and solid symbols, respectively.

DD-PC1 (solid blue circles) [34].

For the Ce isotopes shown in panel (a), nuclei around $N = 82$ are spherical, whereas the remaining nuclei are deformed. Therefore, the spherical and deformed results coincide around $N = 82$. For PCF-PK1, the proton shell gap at $N = 82$ reproduces the experimental data very well. For deformed nuclei, the shell gaps are slightly underestimated within the spherical approximation; including deformation increases the shell gaps and yields better agreement with experiment. In the case of DD-PC1, the shell gaps are close to the experimental data below $N = 82$, and deformation does not change the results. Above $N = 82$, however, the shell gaps are overestimated by about 1 MeV. Deformation plays an important role in this region, substantially reducing the shell gap and, for some nuclei, even bringing it below the experimental data. For PC-PK1, the overestimation of the proton shell gap above $N = 82$ is less severe than in the DD-PC1 case. However, including deformation substantially worsens the results for $N = 90$–98, leading to a severe underestimation of the data.

For U isotopes, the spherical calculation with PCF-PK1 already reproduces the experimental data, albeit with a slight overestimation. Including deformation leads to a further slight reduction in the shell gaps, except for the spherical nuclei at $N = 128$ and 130, and provides a better description than the spherical case. For DD-PC1, the shell gaps in the spherical calculations exhibit large discrepancies of about 2.5 MeV along the entire chain, implying the presence of a spurious $Z = 92$ shell. Between $N = 128$ and 134, the nuclei are predicted to be nearly spherical in the deformed calculations, resulting in a similar deviation of about 2.5 MeV. For $N > 134$, the nuclear shapes become prolate, and the shell gaps gradually decrease, following the trend of PCF-PK1. For PC-PK1, the shell gaps under the spherical approximation are slightly lower than those obtained with DD-PC1, but still show relatively large discrepancies of about 2.5 MeV. Similar to the DD-PC1 case, the deviations in the DRHBc calculations with PC-PK1 remain large below $N = 134$ but diminish with increasing neutron number.

C. Superheavy Nuclei

To further examine the predictive power of PCF-PK1 in the superheavy nuclear region, we show in Fig. 9 the δ_{2n} (a) and δ_{2p} (b) values for nuclei with $Z = 100$ to 140 obtained from DRHFB calculations. The corresponding SRHFB results are also plotted for comparison in panels (c) and (d), respectively. Note that the δ_{2p} values for nuclei with $Z = 140$ are not shown in panel (b), because the ground-state properties of the $Z = 142$ chain have not been calculated in the present work.

For δ_{2n} in the upper panel (a), the DRHFB calculations show local maxima at $N = 162$ for $Z = 100$–110, $N = 184$ for $Z = 100$–122, and $N = 308$ for $Z = 130$–140. In our calculations, the nuclei are spherical at $N = 184, 308$ and prolate at $N = 162$. The magic numbers $N = 162, 184$ are also prominent in the DRHBc calculations with PC-PK1 [41] and the DRHB calculations with DD-PC1 [35].

Compared with the spherical case in panel (c), a deformed magic number emerges at $N = 162$, whereas the magic number at $N = 228$ disappears. In this region, the nuclei are prolate with $\beta_2 \approx 0.2$ for $Z = 100$–128. The

CPC Accepted

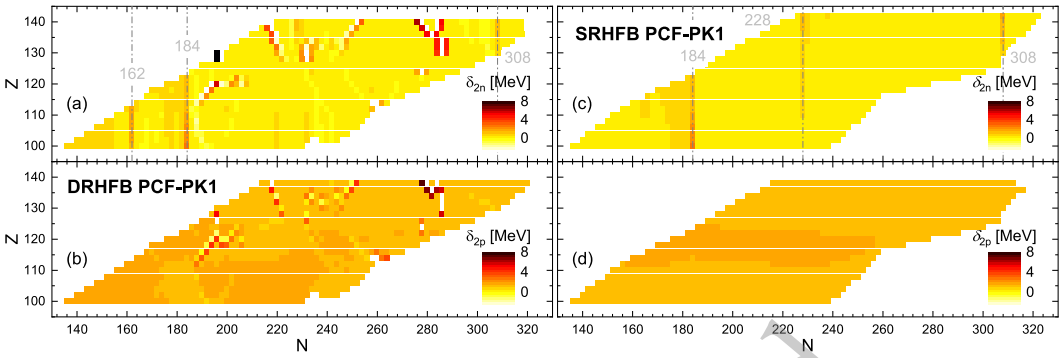

Fig. 9. (color online) Neutron [panels (a)(c)] and proton [panels (b)(d)] shell gaps calculated by DRHFB [panels (a)(b)] and SRHFB [panels (c)(d)][50] using PCF-PK1 interaction.

magnitude of the $N = 184$ gap in the deformed calculations is larger than that in the spherical case for $Z = 100-112$, but becomes smaller for $Z > 112$. Moreover, the magnitude of the $N = 308$ gap in the deformed calculations is consistently smaller than that in the spherical case. Since δ_{2n} and δ_{2p} are influenced by many factors, such as nuclear deformation and pairing effects [35, 91], negative shell gaps appear in the calculations owing to deformation changes, as indicated by the blank at $Z = 134, N = 220$. In addition, some isolated peaks, such as $(Z = 128, N = 196)$, are associated with abrupt changes in nuclear deformation.

In the lower panel (b), δ_{2p} exhibits a pattern quite different from that in panel (a). Since all δ_{2p} values in the DRHFB calculations, except for some isolated peaks, are approximately 2 MeV in this mass region, no obvious proton magic number is predicted in the present work, consistent with the spherical calculations.

Q_α has been used to identify signals of the deformed magic number $N = 162$ in the doubly magic nucleus ^{270}Hs [92]. We plot in Fig. 10 the Q_α values obtained from the spherical and deformed RHFB calculations with PCF-PK1 (orange stars) and from the RCHB and DRHBc calculations with PC-PK1 (blue circles), where open symbols denote spherical results and solid symbols denote deformed results. Note that $E_{\rm rot}$ is considered in the deformed results. The experimental data are indicated by squares, with solid and open squares denoting measured and evaluated values, respectively.

In the spherical calculations, both PCF-PK1 and PC-PK1 exhibit incorrect behavior for Hs isotopes, with Q_α consistently decreasing with increasing neutron number. Under the spherical approximation, the values obtained with PCF-PK1 are closer to the experimental data than those obtained with PC-PK1. When deformation effects are taken into account, the trend of the PCF-PK1 results follows the experimental data closely, except for nuclei around $N = 162$. The local minimum at $N = 162$ obtained with PC-PK1 agrees with the experiment. However, PCF-PK1 overestimates it by about 0.6 MeV, which, combined with the lower peak at $N = 164$, leads to a weaker

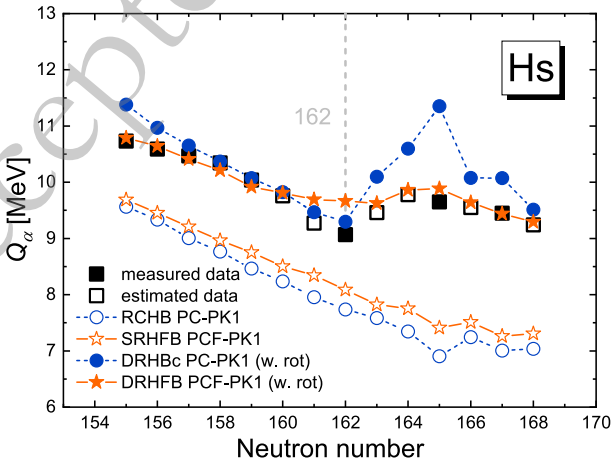

Fig. 10. (color online) The α-decay energies Q_α calculated by DRHFB with PCF-PK1 (solid orange stars) for Hs isotopes are plotted as a function of neutron number. For comparison, the spherical RHFB (open orange stars) calculations with the same functional [50], RCHB calculations with PC-PK1 (open blue circles) [26], as well as the DRHBc calculations with PC-PK1 (solid blue circles) [41] are also displayed. The rotational corrections are considered in the deformed results. The experimental data [92] are denoted by black squares, with solid and open squares indicating measured and evaluated values, respectively. The neutron magic number $N = 162$ is marked by a grey dashed line.

gap at $N = 162$ than that obtained with PC-PK1. Without $E_{\rm rot}$, the PCF-PK1 result for Q_α at $N = 162$ overestimates the experimental value by only 0.25 MeV, as does PC-PK1. Meanwhile, the difference in Q_α between $N = 162$ and 164 is closer to the experiment than that given by PC-PK1. This feature can be understood from the fact that the δ_{2n} value in Fig. 9 is only 1.85 MeV for PCF-PK1, whereas PC-PK1 gives 2.76 MeV.

In addition, the experimental data exhibit a peak at $N = 164$, whereas both the DRHFB calculations with PCF-PK1 and the DRHBc calculations with PC-PK1 place the peak at $N = 165$. However, the Q_α values at $N = 164$ and 165 obtained from the DRHFB calculations

CPC Accepted

with PCF-PK1 are similar, and both agree well with the experimental data, with overestimates of only 0.1 and 0.2 MeV, respectively. In contrast, the PC-PK1 results overestimate this peak by 0.8 MeV, with an even larger discrepancy at $N = 165$.

For Hs isotopes, PCF-PK1 achieves better agreement with the experimental data, with a deviation of 0.2 MeV, whereas the deviation of the PC-PK1 result is 0.7 MeV. Beyond this isotopic chain, PCF-PK1 generally yields a smaller $\sigma = 0.33$ MeV in the superheavy nucleus region with $104 \le Z \le 118$, compared with 1.00 MeV for the PC-PK1 results.

V. IMPROVEMENT OF NUCLEAR MASS PREDICTION WITH NEURAL NETWORK

The DRHFB calculations with PCF-PK1 provide a systematic microscopic description of nuclear masses, but their global accuracy remains limited. The rms deviation of the calculated binding energies without rotational correction from AME2020 is about 2.88 MeV, which is insufficient for *r*-process nucleosynthesis simulations, where nuclear masses with uncertainties of a few hundred keV or less are often required [93]. The residuals between the calculations and experimental data also exhibit systematic and regional trends, indicating that part of the deviation is correlated and cannot be eliminated by the mean-field description alone. Machine-learning techniques provide a means of correcting such residuals, and their performance depends sensitively on the network design. Previous studies have shown that, by incorporating sequential correlations among nuclei, recurrent neural networks (RNNs) can reduce the root-mean-square deviation of nuclear mass predictions to below 100 keV [94]. Anisotropic kernel ridge regression (AKRR) also exploits correlations along isotopic and isotonic chains through a cross-shaped kernel, achieving an rms deviation of 141 keV for WS4-based mass predictions in leave-one-out cross-validation [95]. This result highlights the importance of nuclear-chain correlations. On this basis, we further employ a gated recurrent unit (GRU) architecture to examine the influence of different recurrent units on the description of mass correlations along isotopic and isotonic chains. Compared with a conventional RNN, the GRU introduces update and reset gates to regulate the retention and updating of historical information, thereby providing an alternative recurrent architecture for modeling sequential correlations in nuclear masses. Therefore, in this section, the GRU neural-network approach is used to learn and correct these systematic residuals, with the DRHFB calculations with PCF-PK1 serving as the physical baseline, with the aim of further improving nuclear mass accuracy.

The experimental nuclear masses are taken from AME2020 [9]. Nuclei with $Z \ge 8$ and $N \ge 8$ and experimental mass uncertainties smaller than 100 keV are selected, resulting in a dataset of 2269 nuclei.

Each nucleus is represented by the input vector

$$\boldsymbol{x} = \left(Z, N, \delta, P, A^{1/3}, \Delta_{NZ}, C\right), \tag{41}$$

where Z and N denote the proton and neutron numbers, respectively. The pairing-related quantities are defined as $\delta = [(-1)^Z + (-1)^N]/2$ and $P = v_p v_n/(v_p + v_n)$, where v_p and v_n are the numbers of valence protons and neutrons relative to the nearest closed shells. The neutron-proton asymmetry and Coulomb terms are given by $\Delta_{NZ} = |N - Z|$ and $C = Z(Z-1)/A^{1/3}$, respectively. Here, $A = Z + N$ denotes the mass number.

The deformed relativistic Hartree-Fock-Bogoliubov calculations based on PCF-PK1 are used as the theoretical mass baseline. The network is trained to learn the residuals between the theoretical and experimental binding energies,

$$\Delta E(Z,N) = E_{\mathrm{DRHFB}}(Z,N) - E_{\mathrm{exp}}(Z,N), \tag{42}$$

and the final binding energy is reconstructed as $E_{\mathrm{pred}} = E_{\mathrm{DRHFB}} - \Delta E_{\mathrm{pred}}$.

As shown in Fig. 11, nuclear information is propagated in four directions: increasing N, decreasing N, increasing Z, and decreasing Z. These four pathways enable the model to learn the evolution of nuclear masses along both isotopic and isotonic chains.

For example, in the increasing-N direction, the GRU propagation is expressed as

$$\begin{aligned}
\boldsymbol{r}_{N+} &= \sigma\left(\boldsymbol{W}_{r,N+}\boldsymbol{x} + \boldsymbol{U}_{r,N+}\boldsymbol{h}_{N-1} + \boldsymbol{b}_{r,N+}\right),\\
\boldsymbol{z}_{N+} &= \sigma\left(\boldsymbol{W}_{z,N+}\boldsymbol{x} + \boldsymbol{U}_{z,N+}\boldsymbol{h}_{N-1} + \boldsymbol{b}_{z,N+}\right),\\
\widetilde{\boldsymbol{h}}_{N+} &= \tanh\left[\boldsymbol{W}_{h,N+}\boldsymbol{x} + \boldsymbol{U}_{h,N+}(\boldsymbol{r}_{N+} \odot \boldsymbol{h}_{N-1}) + \boldsymbol{b}_{h,N+}\right],\\
\boldsymbol{h}_{N+} &= (1 - \boldsymbol{z}_{N+}) \odot \boldsymbol{h}_{N-1} + \boldsymbol{z}_{N+} \odot \widetilde{\boldsymbol{h}}_{N+}.
\end{aligned} \tag{43}$$

Here, $\boldsymbol{r}_{N+}$ and $\boldsymbol{z}_{N+}$ denote the reset and update gates, respectively; σ is the sigmoid activation function; and $\odot$ denotes element-wise multiplication. $\boldsymbol{W}$ and $\boldsymbol{U}$ denote the input and recurrent weight matrices, respectively, and $\boldsymbol{b}$ denotes the bias vector. $\widetilde{\boldsymbol{h}}$ and $\boldsymbol{h}$ represent the candidate and updated hidden states, respectively. The subscript $N+$ denotes the direction of increasing neutron number, whereas r, z, and h distinguish the reset gate, update gate, and hidden-state parameters. The decreasing-N, increasing-Z, and decreasing-Z pathways follow the same GRU structure, with independent parameters.

Each GRU pathway contains 30 hidden units and is followed by a 20-neuron linear layer and an output layer. The four pathways independently generate the residual predictions ΔE_{N+}, ΔE_{N-}, ΔE_{Z+}, and ΔE_{Z-}. The two pre-

CPC Accepted

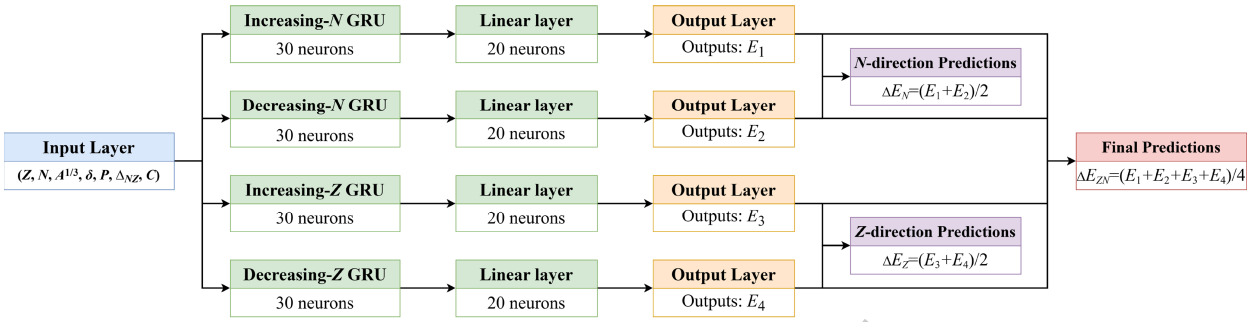

Fig. 11. (color online) Schematic illustration of the four-direction GRU framework for nuclear mass prediction. Nuclear information is propagated independently in the increasing-N, decreasing-N, increasing-Z, and decreasing-Z directions. The two predictions along each coordinate axis are first averaged to obtain the N- and Z-direction predictions, which are then combined to obtain the final mass-residual prediction.

dictions along each coordinate direction are first averaged as $\Delta E_N = (\Delta E_{N+} + \Delta E_{N-})/2$ and $\Delta E_Z = (\Delta E_{Z+} + \Delta E_{Z-})/2$. The final residual prediction is obtained as

$$\Delta E_{\rm pred} = \frac{\Delta E_{N+} + \Delta E_{N-} + \Delta E_{Z+} + \Delta E_{Z-}}{4}. \tag{44}$$

To incorporate correlations beyond one-dimensional isotopic and isotonic chains, we further introduce local correlations with surrounding nuclei during training. For each nucleus (Z,N), a 5×5 region centered on that nucleus is considered. After excluding the central nucleus, up to 24 neighboring nuclei are included, corresponding to $-2 \le \Delta Z, \Delta N \le 2$ with $(\Delta Z, \Delta N) \ne (0,0)$.

For each available central–neighbor pair, the network is constrained to reproduce the difference between their mass residuals, $\Delta E(Z,N) - \Delta E(Z+\Delta Z, N+\Delta N)$. The neighboring-nucleus loss is defined as

$$L_{\rm neighbor} = \frac{1}{N_{\rm pair}} \sum_{(i,j)} \Big[\left(\Delta E_i^{\rm pred} - \Delta E_j^{\rm pred}\right) - \left(\Delta E_i^{\rm exp} - \Delta E_j^{\rm exp}\right) \Big]^2, \tag{45}$$

where $N_{\rm pair}$ denotes the total number of valid neighboring pairs included in the loss evaluation. $\Delta E_i^{\rm pred}$ and $\Delta E_i^{\rm exp}$ denote the predicted and target residuals of nucleus i, respectively, with $\Delta E_i^{\rm exp} = E_{{\rm DRHFB},i} - E_{{\rm exp},i}$. The loss is averaged over all valid neighboring pairs. Because all 24 neighboring offsets are considered, both orientations of each pair are included. The neighboring-nuclei loss is evaluated only when both nuclei in the corresponding pair belong to the training set, thereby avoiding information leakage between the training and validation sets.

The final residual prediction is directly supervised by the experimental residual through $L_{\rm center}$. In addition, the N- and Z-direction predictions are separately constrained by the experimental values, with $L_{\rm direction} = (L_N + L_Z)/2$. The total loss is

$$L = 0.8L_{\rm center} + 0.2L_{\rm neighbor} + 0.10L_{\rm direction} + L_{\rm reg}, \tag{46}$$

The center and directional losses are defined as follows:

$$L_{\rm center} = \frac{1}{N_c}\sum_{i=1}^{N_c}(\Delta E_i^{\rm pred} - \Delta E_i^{\rm exp})^2,$$
$$L_N = \frac{1}{N_c}\sum_{i=1}^{N_c}(\Delta E_{N,i} - \Delta E_i^{\rm exp})^2,$$
$$L_Z = \frac{1}{N_c}\sum_{i=1}^{N_c}(\Delta E_{Z,i} - \Delta E_i^{\rm exp})^2, \tag{47}$$

where N_c denotes the number of training nuclei included in the loss evaluation. $\Delta E_{N,i}$ and $\Delta E_{Z,i}$ are the predictions averaged over the increasing and decreasing pathways in the N and Z directions, respectively. $L_{\rm center}$ constrains the final residual prediction, whereas L_N and L_Z separately constrain the two directional predictions, thereby reducing compensating errors between them.

The regularization term is defined as

$$L_{\rm reg} = \lambda \sum_{\boldsymbol{W}\in\mathcal{W}} \|\boldsymbol{W}\|_F^2, \qquad \lambda = 10^{-4}, \tag{48}$$

where $\mathcal{W}$ denotes the set of regularized weight matrices, which include the input and recurrent weights of the GRU layers and the weights of the fully connected and output layers. $\|\boldsymbol{W}\|_F^2$ denotes the sum of the squared matrix elements. All supervised loss terms are evaluated using only the training nuclei. These choices were based on a coarse preliminary scan; the final performance was found to be insensitive to small changes in these weights. During validation, only the center loss is evaluated. The model parameters are optimized using the Adamax optimizer. A five-fold cross-validation strategy is employed for the 2269 selected nuclei from AME2020 with $Z \ge 8$, $N \ge 8$,

CPC Accepted

and experimental mass uncertainties below 100 keV. The dataset is randomly partitioned into five subsets. In each fold, four subsets, corresponding to approximately 80% of the nuclei, are used for training, whereas the remaining subset is used for validation. Thus, each nucleus is used once for validation over the five folds. To reduce the influence of random initialization, each fold is trained independently 100 times with different random initializations, and the predictions from these 100 runs are averaged to obtain the fold-specific prediction. The final prediction for each nucleus is obtained by averaging the predictions from all five folds.

Fig. 12 compares the deviations between the predicted and experimental nuclear binding energies obtained with DRHFB PCF-PK1 and the GRU. The blue symbols represent the DRHFB PCF-PK1 calculations, whereas the red symbols denote the GRU results. For the 2269 nuclei used in model development, the rms deviation of DRHFB PCF-PK1 is 2.883 MeV, whereas the final averaged GRU predictions yield an rms deviation of 0.089 MeV, corresponding to a reduction of approximately 96.9%. The overall distribution shows that the DRHFB PCF-PK1 residuals exhibit noticeable systematic variations across different nuclear regions, whereas the GRU-corrected results are more tightly clustered around zero, with the large-scale residual structures substantially suppressed.

The continuous variation of the DRHFB PCF-PK1 residuals indicates that the differences between theory and experiment exhibit strong local correlations among neighboring nuclei. In the present framework, the four-directional GRU extracts the evolution of mass residuals along both isotopic and isotonic chains, while the additional constraint involving the 24 surrounding nuclei further incorporates local correlations across the two-dimensional nuclear chart. This enables the network to effectively correct the systematic components contained in the DRHFB PCF-PK1 residuals.

The two horizontal dashed lines in Fig. 12 indicate deviations of ±1 MeV from the experimental values. Accuracy at the level of several hundred keV or better is particularly relevant for nuclear-structure studies and for nuclear-mass inputs in *r*-process calculations. Of the 2269 nuclei considered, the GRU predictions for 1801 differ from experiment by less than 100 keV, corresponding to 79.37%. When the deviation range is extended to 200 keV, this fraction increases to 96.12%, corresponding to 2181 nuclei. Only two nuclei show deviations larger than 500 keV, indicating that 99.91% of the nuclei are reproduced within 500 keV. For comparison, only 179 nuclei in the DRHFB PCF-PK1 calculations have deviations smaller than 500 keV. The mean absolute error of the GRU predictions is only 0.0645 MeV, consistent with the strong compression of the overall error distribution.

A nucleus-by-nucleus comparison further shows that

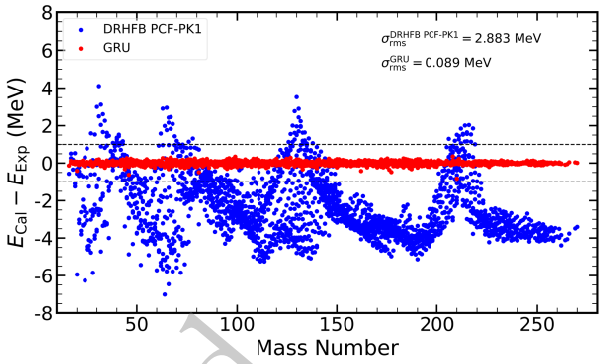

Fig. 12. (color online) Deviations between the predicted and experimental nuclear binding energies for DRHFB PCF-PK1 and GRU. The blue symbols represent the DRHFB PCF-PK1 calculations, while the red symbols denote the GRU predictions. The two horizontal dashed lines indicate deviations of ±1 MeV from the experimental values. The corresponding rms deviations are also shown in the figure.

only 17 of the 2269 nuclei are not improved by the GRU correction, whereas the predictions for the remaining 2252 nuclei are closer to the experimental values than the corresponding DRHFB PCF-PK1 results, accounting for 99.25% of the dataset. This demonstrates that the improvement is not dominated by a small number of nuclei but is achieved systematically across almost the entire dataset.

The only nuclei for which the GRU deviations exceed 500 keV are ^{46}V and ^{210}Bi. For these two nuclei, the residuals between DRHFB PCF-PK1 and experiment show weaker local smoothness along both the corresponding isotopic and isotonic chains, making the sequential correction more difficult.

To further assess the extrapolation capability, we selected 64 nuclei excluded from GRU training based on the new experimental mass data compiled in Ref. [96]. For these nuclei, the GRU yields an rms deviation of 0.3453 MeV, slightly lower than the 0.3577 MeV obtained with WS4 [11]. These results provide support for the model's predictive capability for nuclei not used in model development.

VI. SUMMARY

In summary, we have extended the RHFB calculations based on the density-dependent point-coupling functional PCF-PK1 from the spherical approximation to an axially deformed framework, in which the exchange terms are incorporated through the Fierz transformation. Systematic DRHFB calculations have been performed for nuclei with $8 \le Z \le 120$, providing a deformed mass table for 7550 nuclei predicted to be bound.

The inclusion of deformation substantially improves the description of basic ground-state properties. The rms

CPC Accepted

deviation of the binding energies with respect to the 2373 experimental data points is reduced to 2.882 MeV, and further to 1.721 MeV when $E_{\rm rot}$ is included, indicating an improvement of about 0.4 MeV relative to the RMF+BCS results with the TMA interaction. Compared with the spherical case, the predicted drip-line positions agree better with experiment, with rms deviations of 2.65 for neutrons and 1.18 for protons. The charge radii are also reproduced more accurately, with the rms deviation decreasing to 0.0298 fm, about 19% smaller than that of the DRHBc calculation with PC-PK1 for even-Z nuclei. The α-decay energies are also substantially improved, with the rms deviation of Q_α decreasing to 0.7215 MeV, but slightly increasing to 0.7511 MeV when $E_{\rm rot}$ is included.

The shell structures are further examined through the two-nucleon shell gaps. The traditional magic numbers $N = 8$, 20, 50, 82, and 126 are reproduced, and $N = 184$ is predicted. In the deformed results, the spurious shell closures at $Z = 58$ and $Z = 92$ remain eliminated, consistent with the spherical calculations. In the superheavy-nucleus region, the neutron magic numbers $N = 162, 184, 308$ are predicted, while no pronounced proton magic number is found in the present work.

To further improve the mass accuracy, a neural-network approach has been adopted to correct the systematic mass residuals between the DRHFB calculations with PCF-PK1 and the experimental data. As a result, the rms deviation of the binding energies is further reduced to 0.089 MeV, corresponding to a reduction of about 96.9%.

DATA AVAILABILITY STATEMENT

The dataset supporting the findings of this study is provided as Supplemental Material and is openly available in Science Data Bank at https://doi.org/10.57760/sciencedb.014n7.

CPC Accepted

References

[1] F. Wienholtz, D. Beck, K. Blaum, *et al.*, Nature **498**, 346 (2013)
[2] M. Wang, Y. H. Zhang, X. Zhou, *et al.*, Phys. Rev. Lett. **130**, 192501 (2023)
[3] Y. M. Xing, Y. F. Luo, Y. H. Zhang, *et al.*, Phys. Rev. Lett. **135**, 012501 (2025)
[4] Y. Yu, Y. M. Xing, Y. H. Zhang, *et al.*, Phys. Rev. Lett. **133**, 222501 (2024)
[5] F. F. Xu, P. W. Zhao, Phys. Rev. Lett. **136**, 232503 (2026)
[6] B. H. Sun, Yu. A. Litvinov, I. Tanihata, *et al.*, Front. Phys. **10**, 1 (2015)
[7] E. M. Burbidge, G. R. Burbidge, W. A. Fowler, *et al.*, Rev. Mod. Phys. **29**, 547 (1957)
[8] M. Arnould, S. Goriely, Prog. Part. Nucl. Phys. **112**, 103766 (2020)
[9] M. Wang, W. J. Huang, F. G. Kondev, *et al.*, Chin. Phys. C **45**, 030003 (2021)
[10] X. Y. Qu, K.-M. Chen, C. Pan, *et al.*, Nucl. Sci. Tech. **36**, 231 (2025)
[11] N. Wang, M. Liu, X. Wu, *et al.*, Phys. Lett. B **734**, 215 (2014)
[12] P. Möller, A. J. Sierk, T. Ichikawa, *et al.*, At. Data Nucl. Data Tables **109-110**, 1 (2016)
[13] T. Yu, Y. Y. Guo, X. F. Jiang, *et al.*, Chin. Phys. C **50**, 054104 (2026)
[14] S. A. Giuliani, G. Martínez-Pinedo, A. Bauswein, *et al.*, Phys. Rev. C **113**, 045806 (2026)
[15] S. Goriely, N. Chamel, J. M. Pearson, Phys. Rev. Lett. **102**, 152503 (2009)
[16] S. Goriely, N. Chamel, J. M. Pearson, Phys. Rev. C **88**, 061302 (2013)
[17] J. Erler, N. Birge, M. Kortelainen, *et al.*, Nature **486**, 509 (2012)
[18] S. Goriely, S. Hilaire, M. Girod, *et al.*, Phys. Rev. Lett. **102**, 242501 (2009)
[19] J. Meng (ed.), *Relativistic Density Functional for Nuclear Structure* (Singapore: World Scientific, 2016)
[20] M. M. Sharma, G. Lalazissis, J. König, *et al.*, Phys. Rev. Lett. **74**, 3744 (1995)
[21] J. Y. Guo, Phys. Rev. C **85**, 021302 (2012)
[22] Z. X. Ren, P. W. Zhao, Phys. Rev. C **102**, 021301 (2020)
[23] H. Z. Liang, J. Meng, S.-G. Zhou, Phys. Rep. **570**, 1 (2015)
[24] W. Koepf, P. Ring, Nucl. Phys. A **493**, 61 (1989)
[25] Z. X. Liu, Y. H. Lam, N. Lu, *et al.*, Phys. Lett. B **842**, 137946 (2023)
[26] X. W. Xia, Y. Lim, P. W. Zhao, *et al.*, At. Data Nucl. Data Tables **121-122**, 1 (2018)
[27] J. Dobaczewski, W. Nazarewicz, J. Skalski, *et al.*, Phys. Rev. Lett. **60**, 2254 (1988)
[28] A. Bohr, B. R. Mottelson, *Nuclear Structure. Volume II. Nuclear Deformations* (Reading, MA: Addison-Wesley/W. A. Benjamin, Inc., 1975)
[29] D. Hirata, K. Sumiyoshi, I. Tanihata, *et al.*, Nucl. Phys. A **616**, 438 (1997)
[30] A. Bohr, B. R. Mottelson, D. Pines, Phys. Rev. **110**, 936 (1958)
[31] G. A. Lalazissis, S. Raman, P. Ring, At. Data Nucl. Data Tables **71**, 1 (1999)
[32] L. S. Geng, H. Toki, J. Meng, Prog. Theor. Phys. **113**, 785 (2005)
[33] A. V. Afanasjev, S. E. Agbemava, D. Ray, *et al.*, Phys. Lett. B **726**, 680 (2013)
[34] S. E. Agbemava, A. V. Afanasjev, D. Ray, *et al.*, Phys. Rev. C **89**, 054320 (2014)
[35] S. E. Agbemava, A. V. Afanasjev, T. Nakatsukasa, *et al.*, Phys. Rev. C **92**, 054310 (2015)
[36] S.-G. Zhou, J. Meng, P. Ring, *et al.*, Phys. Rev. C **82**, 011301 (2010)
[37] L. L. Li, J. Meng, P. Ring, *et al.*, Phys. Rev. C **85**, 024312 (2012)
[38] K. Y. Zhang, M.-K. Cheoun, Y.-B. Choi, *et al.*, Phys. Rev. C **102**, 024314 (2020)
[39] C. Pan, *et al.*, Phys. Rev. C **106**, 014316 (2022)
[40] K. Zhang, M.-K. Cheoun, Y.-B. Choi, *et al.*, At. Data Nucl.

Data Tables **144**, 101488 (2022)
[41] P. Guo, X. Cao, K. Chen, *et al.*, At. Data Nucl. Data Tables **158**, 101661 (2024)
[42] Y. L. Yang, Y. K. Wang, P. W. Zhao, *et al.*, Phys. Rev. C **104**, 054312 (2021)
[43] W. H. Long, H. Sagawa, N. V. Giai, *et al.*, Phys. Rev. C **76**, 034314 (2007)
[44] W. H. Long, H. Sagawa, J. Meng, *et al.*, Europhys. Lett. **82**, 12001 (2008)
[45] J. Geng, J. J. Li, W. H. Long, *et al.*, Phys. Rev. C **100**, 051301 (2019)
[46] H. Z. Liang, P. W. Zhao, P. Ring, *et al.*, Phys. Rev. C **86**, 021302(R) (2012)
[47] Q. Zhao, Z. X. Ren, P. W. Zhao, *et al.*, Phys. Rev. C **106**, 034315 (2022)
[48] L. S. Geng, J. Meng, H. Toki, *et al.*, Chin. Phys. Lett. **23**, 1139 (2006)
[49] B. Wei, Q. Zhao, Z. H. Wang, *et al.*, Chin. Phys. C **44**, 074107 (2020)
[50] Y. N. Huang, Q. Zhao, Y. F. Niu, *Nuclear landscape based on point-coupling density functional with localized exchange terms*, Nucl. Sci. Tech., to be published
[51] B. A. Nikolaus, T. Hoch, D. G. Madland, Phys. Rev. C **46**, 1757 (1992)
[52] T. Bürvenich, D. G. Madland, J. A. Maruhn, *et al.*, Phys. Rev. C **65**, 044308 (2002)
[53] M. Fierz, Z. Phys. **104**, 553 (1937)
[54] P. Manakos, T. Mannel, Z. Phys. A **334**, 481 (1989)
[55] A. Sulaksono, T. Bürvenich, J. A. Maruhn, *et al.*, Ann. Phys. (N.Y.) **306**, 36 (2003)
[56] S. Typel, H. H. Wolter, Nucl. Phys. A **656**, 331 (1999)
[57] P. Ring, P. Schuck, *The Nuclear Many-Body Problem* (Berlin: Springer-Verlag, 1980)
[58] C. Fuchs, H. Lenske, H. H. Wolter, Phys. Rev. C **52**, 3043 (1995)
[59] T. Nikšić, D. Vretenar, P. Finelli, *et al.*, Phys. Rev. C **66**, 024306 (2002)
[60] Y. Tian, Z.-Y. Ma, P. Ring, Phys. Lett. B **676**, 44 (2009)
[61] T. Nikšić, N. Paar, D. Vretenar, *et al.*, Comput. Phys. Commun. **185**, 1808 (2014)
[62] Y. K. Gambhir, P. Ring, A. Thimet, Ann. Phys. (N.Y.) **198**, 132 (1990)
[63] J.-P. Ebran, E. Khan, D. Peña Arteaga, *et al.*, Phys. Rev. C **83**, 064323 (2011)
[64] J. Geng, W. H. Long, Phys. Rev. C **105**, 034329 (2022)
[65] M. Bender, K. Rutz, P.-G. Reinhard, *et al.*, Eur. Phys. J. A **7**, 467 (2000)
[66] P. W. Zhao, Z. P. Li, J. M. Yao, *et al.*, Phys. Rev. C **82**, 054319 (2010)
[67] S. Perez-Martin, L. M. Robledo, Phys. Rev. C **78**, 014304 (2008)
[68] L. L. Li, J. Meng, P. Ring, *et al.*, Chin. Phys. Lett. **29**, 042101 (2012)
[69] K. Y. Zhang, S. Q. Zhang, *et al.*, Phys. Rev. C **108**, L041301 (2023)
[70] K. Y. Zhang, S. Q. Zhang, J. Meng, Phys. Rev. C **112**, 044308 (2025)
[71] K. Heyde, J. L. Wood, Rev. Mod. Phys. **83**, 1467 (2011)
[72] Z. P. Li, T. Nikšić, D. Vretenar, *et al.*, Phys. Rev. C **79**, 054301 (2009)
[73] Y. L. Yang, P. W. Zhao, Z. P. Li, Phys. Rev. C **107**, 024308 (2023)
[74] M. Thoennessen, Rep. Prog. Phys. **67**, 1187 (2004)
[75] Z. Y. Zhang, Z. G. Gan, H. B. Yang, *et al.*, Phys. Rev. Lett. **122**, 192503 (2019)
[76] D. S. Ahn, N. Fukuda, H. Geissel, *et al.*, Phys. Rev. Lett. **123**, 212501 (2019)
[77] Y. L. Yang, P. W. Zhao, http://nuclearmap.jcnp.org/index.html
[78] T. Nikšić, Z. P. Li, D. Vretenar, *et al.*, Phys. Rev. C **79**, 034303 (2009)
[79] M. Bender, G. F. Bertsch, P.-H. Heenen, Phys. Rev. Lett. **94**, 102503 (2005)
[80] M. Bender, G. F. Bertsch, P.-H. Heenen, Phys. Rev. C **73**, 034322 (2006)
[81] C. Pan, K. Y. Zhang, P. S. Chong, *et al.*, Phys. Rev. C **104**, 024331 (2021)
[82] X. T. He, C. Wang, K. Y. Zhang, *et al.*, Chin. Phys. C **45**, 101001 (2021)
[83] K. Zhang, X. He, J. Meng, *et al.*, Phys. Rev. C **104**, L021301 (2021)
[84] X. T. He, J. W. Wu, K. Y. Zhang, *et al.*, Phys. Rev. C **110**, 014301 (2024)
[85] C. Pan, J. Meng, Phys. Rev. C **112**, 024316 (2025)
[86] I. Angeli, K. P. Marinova, At. Data Nucl. Data Tables **99**, 69 (2013)
[87] T. Li, Y. Luo, N. Wang, At. Data Nucl. Data Tables **140**, 101440 (2021)
[88] B. Pritychenko, M. Birch, B. Singh, *et al.*, At. Data Nucl. Data Tables **107**, 1 (2016)
[89] M.-H. Mun, S. Kim, M.-K. Cheoun, *et al.*, Phys. Lett. B **847**, 138298 (2023)
[90] J. P. Delaroche, M. Girod, J. Libert, *et al.*, Phys. Rev. C **81**, 014303 (2010)
[91] A. V. Afanasjev, S. E. Agbemava, D. Ray, *et al.*, Phys. Rev. C **91**, 014324 (2015)
[92] J. Dvorak, W. Brüchle, M. Chelnokov, *et al.*, Phys. Rev. Lett. **97**, 242501 (2006)
[93] M. R. Mumpower, R. Surman, G. C. McLaughlin, *et al.*, Prog. Part. Nucl. Phys. **86**, 86 (2016)
[94] P. Li, Y. F. Niu, F. Q. Chen, *et al.*, arXiv: 2609.13782
[95] X. H. Wu, C. Pan, Phys. Rev. C **110**, 034322 (2024)
[96] X. Y. Qu, K. M. Chen, C. Pan, *et al.*, Nucl. Sci. Tech. **36**, 231 (2025)

CPC Accepted